16th East Asia-Pacific Conference on Structural Engineering & Construction (EASEC16)
Edited by S.T. Quek, D. Kumar and L.H. Poh
Brisbane, Australia, December 3-6, 2019

PETAL AUXETICS WITH TARGETED POISSON'S RATIO USING ISOGEOMETRIC SHAPE OPTIMIZATION

Ser Tong Quek*, Deepak Kumar and Leong Hien Poh

Department of Civil and Environmental Engineering, National University of Singapore, 1Engineering Drive 2, Singapore 117576

Emails: st_quek@nus.edu.sg, pdeepakkumar@u.nus.edu, leonghien@nus.edu.sg

*Corresponding author

Abstract. *Auxetic materials with negative Poisson's ratio have potential applications across a broad range of engineering fields. Several design techniques have been developed to obtain auxetics with targeted mechanical properties. However, many of these finite element based techniques are difficult to use directly for auxetics, particularly during the design optimization stage which involves evolving boundary parts with large curvatures. This paper focusses on a series of smoothed petal auxetics, with lower stress concentrations at connecting parts, compared to the reference star shaped structures. An isogeometric shape optimization framework to achieve target Poisson's ratios at large deformation is presented. Several smoothed petal auxetic designs with target constant Poisson's ratios up to an effective tensile strain of 30% are shown to demonstrate the capability of the optimization framework.*

Keywords: *Auxetic; Negative Poisson's Ratio; Isogeometric analysis; Shape optimization; Sensitivity analysis;*

1. INTRODUCTION

In contrast to conventional materials, auxetics are a class of structural and/or functional materials that expand (contract) transversely when stretched (compressed) in the axial direction, exhibiting a negative Poisson's ratio (NPR) phenomenon (Alderson 1999). This counter-intuitive behavior has been shown to enhance the mechanical properties of engineering structures. Auxetics have thus been a subject of increased interest in recent years.

The deformation mechanisms (Lakes 1991) and mechanical properties of auxetics such as indentation, shear resistance (Alderson et al. 2000, Dirrenberger et al. 2014), energy absorption (Zhu et al. 2018, Zhu et al. 2019) and wave propagation characteristics (Spadoni et al. 2009) have been studied for various engineering applications. Design techniques based on modern numerical methods started with the works of Sigmund (Sigmund 1994, 1995). Subsequently, several design frameworks adopting topology optimization such as Solid Isotropic Material with Penalization (SIMP) (Schwerdtfeger et al. 2011), evolutionary hybrid algorithms (Kaminakis et al. 2015), and Bi-directional Evolutionary Structural Optimization (BESO) (Da et al. 2018, Xia et al. 2018) have been developed for design of auxetic structures. Recently, a level-set based topology optimization was successfully employed to obtain designs with prescribed Poisson's ratios in the elastic regime (Vogiatzis et al. 2017, Wang et al. 2017a).

Although auxetics are subjected to large deformation in many potential applications, the above-mentioned design approaches are limited to the linear regime. Experimental results have shown that auxetics exhibit significant nonlinear behavior at finite strains (Alderson et al. 2000, Smith et al. 1999). Consequently, the optimized effective properties based on linear theory may degrade rapidly with deformation (Clausen et al. 2015, Wang et al. 2014a). To overcome this, topology optimization is adopted for the design of auxetics with prescribed non-linear properties at finite strains (Clausen et al. 2015, Wang et al. 2014a).

However, most published numerical optimization frameworks for auxetics are based on the finite element (FE) framework. In general, a FE based structural optimization framework is time consuming because of the need to ensure a proper integration between the geometrical description and the corresponding FE analysis (Lian et al. 2016). Moreover, approximating the design domain with FE meshes reduces the accuracy of the geometrical description (Xie et al. 2018). To this end, an isogeometric shape optimization framework for smoothed petal auxetics was presented in Wang et al. (2017b). Subsequently, isogeometric shape optimization was employed to design planar isotropic auxetics with prescribed effective properties in the linear regime (Wang and Poh 2018) and prescribed Poisson's ratios in the nonlinear regime (Choi and Cho 2018, Weeger et al. 2019). In this paper, the isogeometric shape optimization for petal auxetics is extended for achieving targeted effective properties in the nonlinear deformation regime. The versatility of the presented approach is demonstrated by designing petal auxetic structures with constant NPRs within -0.5, considering both plane strain and plane stress conditions, in the strain interval [0.00, 0.30].

2. ISOGEOMETRIC ANALYSIS FOR SMOOTHED PETAL AUXETICS

The auxetic behavior of star shaped re-entrant structures has been studied by several researchers. The auxeticity of such structures is found to depend largely on hinge-functional connections at the vertex connections (Carneiro et al. 2016). This poses a great challenge in manufacturing and may lead to significant stress concentrations. Consequently, a series of petal auxetics with smoothed connections, was proposed in Wang et al. (2017b). This study focusses on such smoothed petal auxetics that are amenable to the manufacturing process and exhibit lower stress concentrations, compared to the reference star shaped structures.

As highlighted in Wang et al. (2017b), a key challenge for the shape optimization of petal auxetics is the proper integration between the curved geometrical description and the corresponding FE analysis. The isogeometric analysis (IGA) (Hughes et al. 2005) integrates the analysis and design processes together. IGA is thus well suited for shape optimization in terms of the exact geometrical description and enhanced sensitivity analysis (Cho and Ha 2009, Wall et al. 2008). In IGA, the control points representing the design boundary of the geometry can directly serve as optimization variables, thus eliminating the need for re-meshing (Sun et al. 2018, Weeger et al. 2019).

In the following, the IGA framework for smoothed petal auxetics in the nonlinear deformation regime is presented.

2.1. Initial Shape Setting and Updating Scheme

The shape updating scheme for smoothed petal auxetics presented in Kumar et al. (2019), is summarized as follows. Commencing from reference petal-shaped structures shown in Fig. 1, this study seeks an optimized geometry which achieves a targeted Poisson's ratio in the nonlinear deformation regime. The entire geometry can be obtained through the patterning of one petal, henceforth termed as *parent petal* and addition of connecting bars. To simplify the design problem, only the exterior boundary of the design problem is considered. The control points defining the exterior boundary of the parent petal are thus chosen as design variables.

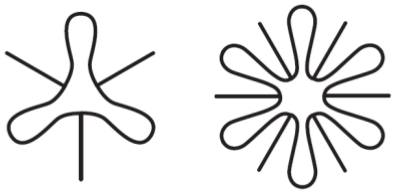

Figure 1. Smoothed tri- and hexa- petals auxetic structures.

The initial parent petal characterization starts with the description of its interior boundary by considering practical engineering and manufacturing prerequisites. Next, the control points of the interior boundary are simply offset to obtain the initial exterior boundary of the parent petal. A closed boundary for parent petal is formed by connecting the interior and exterior boundaries via straight lines at the planes of symmetry. Henceforth, the space where the parent petal is characterized is called *design space*. The external boundary of the petal will be updated during the iterative process of the optimization framework.

2.2. Characterization of Nonlinear Deformation

In this study, a biocompatible silicone-based rubber (commercial name: Elite Double 32, Zhermack) is considered as the base material. The Yeoh hyperelastic model (Yeoh 1993) is adopted to characterize the nonlinear response. Following Yeoh (1993), the strain energy density is given as

$$\psi(F) = C_1(\overline{I_1} - 3) + C_2(\overline{I_1} - 3)^2 + C_3(\overline{I_1} - 3)^3 + \frac{1}{D_1}(J-1)^2 + \frac{1}{D_2}(J-1)^4 + \frac{1}{D_3}(J-1)^6, \tag{1}$$

where C_i and D_i are material parameters $(i = 1,2,3)$. Here, $\overline{I_1} = J^{-\frac{2}{3}} tr[\boldsymbol{F}\boldsymbol{F}^T]$ is the first invariant for incompressible material, $J = \det(\boldsymbol{F})$ and $\boldsymbol{F}$ is the deformation gradient. For the silicone-based rubber base material, $C_1 = 131\ KPa$, $C_2 = 0\ KPa$, $C_3 = 3.5\ KPa$, $D_1 = D_2 = D_3 = 154\ GPa^{-1}$ (Babaee et al. 2013).

The first Piola-Kirchioff stress ($\boldsymbol{P}$) can be obtained as

$$P_{ij} = \frac{\partial\psi}{F_{ij}} = 2\,C_1 J^{-\frac{2}{3}}\left[F_{ij} - \frac{1}{3}I_1 F_{ij}^{-T}\right] + 4\,C_2 J^{-\frac{2}{3}}(\overline{I_1} - 3)\left[F_{ij} - \frac{1}{3}I_1 F_{ij}^{-T}\right] + 6\,C_3 J^{-\frac{2}{3}}(\overline{I_1} - 3)^2\left[F_{ij} - \frac{1}{3}I_1 F_{ij}^{-T}\right] + \frac{2}{D_1}(J-1)\,J\,F_{ij}^{-T} + \frac{4}{D_2}(J-1)^3\,J\,F_{ij}^{-T} + \frac{6}{D_3}(J-1)^3\,J\,F_{ij}^{-T}\ . \tag{2}$$

The paper focuses on achieving prescribed NPRs in the large deformation regime. The deformation of representative volume element (RVE) shown in Fig. 2 is characterized via the average Biot strain (Biot 1939) defined as

$$\boldsymbol{E} = \sqrt{\boldsymbol{F}^T\boldsymbol{F}} - \boldsymbol{1} \tag{3}$$

where $\boldsymbol{1}$ is the second-order identity tensor. In the following, the fine scale analysis within a RVE is termed as “micro”, and the effective response of a RVE as “macro”.

Within a RVE, the bulk material forming the structure occupies a sub-domain $\Omega \subset V$ with boundary Γ. This structure characterized by region Ω is the design object, while the rest of the RVE is empty. The updated designs of region Ω in an iterative design process, can be considered as a sequence that follows a time-like parameter τ (Choi and Kim 2016).

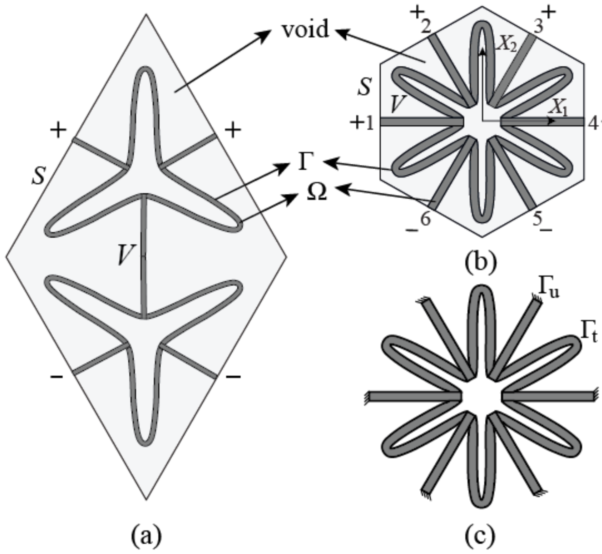

Figure 2. RVE of smoothed (a) tri-petals structure and (b) hexa-petals structure. (c) Traction and displacement boundaries, $\Gamma = \Gamma_t + \Gamma_u$.

Following the standard homogenization procedure, a boundary value problem (BVP) for the microstructure in material configuration with a Biot (macro) strain $\boldsymbol{E}$ can be obtained by imposing periodic boundary conditions and is given by,

$$\begin{cases} \boldsymbol{c}[\boldsymbol{u}] \coloneqq \operatorname{div} \boldsymbol{P} = \boldsymbol{0} & \text{in } \Omega^{\tau} \\ \hat{\boldsymbol{t}} = \boldsymbol{0} & \text{on } \Gamma_t^{\tau} \\ \boldsymbol{x}^{+} - \boldsymbol{x}^{-} = \boldsymbol{F} \cdot (\boldsymbol{X}^{+} - \boldsymbol{X}^{-}) & \text{on } \Gamma_u^{\tau} \end{cases} \tag{4}$$

where $\boldsymbol{P}$ denotes the first Piola-Kirchoff stress tensor, with symbols '+' and '-' denoting the opposing sides of a RVE.

2.3. Isogeometric Discretization

Non-uniform Rational B-Splines (NURBS) offer great flexibility in modelling smoothed petal auxetics with the combination of control points located in the physical space and the basis function defined in the index space (Nguyen et al. 2019). The isogeometric shape optimization adopts the locations and weights of the control points as design variables. Hence, it allows the smooth shape variation of petal auxetics during an iterative design process.

A general expression for a NURBS surface with parameters ξ and η is expressed mathematically as

$$\boldsymbol{X}[\xi,\eta] = \sum_{i=1}^{n} \sum_{j=1}^{m} R^{ij}\,[\xi,\eta]\boldsymbol{X}^{ij}, \tag{5}$$

where $n \times m$ control points denoted by $\boldsymbol{X}^{ij}$ form a control net and R^{ij} represents the NURBS basis function. Based on the non-decreasing knot vectors $\boldsymbol{\xi} = \{\xi_1, \xi_2, \xi_3, \ldots \xi_{n+p+1}\}$ and $\boldsymbol{\eta} = \{\eta_1, \eta_2, \eta_3, \ldots \eta_{n+p+1}\}$, the NURBS basis function R^{ij} can be defined as

$$R^{ij}[\xi,\eta] = \frac{N^{i,p}[\xi]M^{j,q}[\eta]w^{i,j}}{\sum_{i'=1}^{n}\sum_{j'=1}^{m} N^{i',p}[\xi]M^{j',q}[\eta]w^{i',j'}} \tag{6}$$

where $N^{i,p}[\xi]$ and $M^{j,q}[\eta]$ are the B-spline basis functions, $w^{i,j}$ is the weight of control point $\boldsymbol{X}^{ij}$, p and q denote the degrees in the parametric axes ξ and η, respectively.

In IGA, the displacement fields are discretized using NURBS parametrization as follows:

$$\boldsymbol{u}[\xi,\eta] = \sum_{i=1}^{n} \sum_{j=1}^{m} R^{ij}\,[\xi,\eta]\boldsymbol{u}^{ij}, \tag{7}$$

where $\boldsymbol{u}^{ij}$ is the displacement corresponding to the control point $\boldsymbol{X}^{ij}$.

The static equilibrium of a RVE is governed by the following equation:

$$\boldsymbol{r} = \boldsymbol{f}^{ext} - \boldsymbol{f}^{int}(\boldsymbol{u}) = 0, \tag{8}$$

where $\boldsymbol{r}$ is the residual force vector, $\boldsymbol{f}^{ext}$ is the external force vector, and $\boldsymbol{f}^{int}(\boldsymbol{u})$ is the internal force vector.

The static equilibrium given by Eq. (8), is solved iteratively using the Newton-Raphson method to give

$$\underline{\underline{K_t}}\,\underline{du} = \underline{r}, \tag{9}$$

where $\underline{du}$ is the correction displacement vector and $\underline{\underline{K_t}}$ is the tangent stiffness matrix.

The NURBS model is discretized differently for efficient analysis and design in the context of isogeometric shape optimization. In the design space, a coarse discretization is used to minimize the number of design variables whereas a refined discretization is employed in the analysis space to accurately compute the state fields (Lian et al. 2017).

3. OPTIMIZATION FORMULATION FOR 2D AUXETIC DESIGN

In this section, an isogeometric shape optimization framework for achieving the prescribed Poisson's ratios at large deformation is presented. The optimization is performed using "fmincon" function in MATLAB, which necessitates computation of design objective, constraints and their gradients with respect to design variables.

3.1. Design Objective and Sensitivity Analysis

The aim is to find the optimized shape of the design boundary, such that the prescribed Poisson's ratios can be achieved. For the petal auxetics, it is also desirable to preserve the geometrical symmetry. Correspondingly, the objective function can be defined as the minimization of least square difference between the actual and targeted Poisson's ratios, given as

$$\Phi \coloneqq \sum_{\alpha=1}^{\beta}(\nu - \bar{\nu})_{\alpha}^{2} = \sum_{\alpha=1}^{\beta}\frac{1}{(E_{11})_{\alpha}^{2}}\left(E_{22} - \overline{E_{22}}\right)_{\alpha}^{2} \tag{10}$$

where E_{22} and $\bar{E}_{22}$ are the actual and targeted transverse strains at a given applied longitudinal strain (E_{11}), and β is the number of target strains to achieve.

To simplify the sensitivity analysis, the objective function can be reformulated as

$$\Phi \coloneqq \sum_{\alpha=1}^{\beta}\left\{\sum_{k}\frac{1}{E_{11}}\left(\frac{u_2^{(k)} - \bar{u}_2^{(k)}}{X_2^{(k)}}\right)\right\}_{\alpha}^{2} = \sum_{\alpha=1}^{\beta}\left\{\sum_{k}\frac{1}{(E_{11}W)^2}\left(u_2 - \bar{u}_2\right)_{k}^{2}\right\}_{\alpha}, \tag{11}$$

where $X_1^{(k)}$ and $X_2^{(k)}$ are the X_1- and X_2-coordinates of the master control point k, respectively and $W = X_2^{(k)}$ (refer Fig. 2). The actual and targeted displacements of master control point k are denoted by $u_2^{(k)}$ and $\bar{u}_2^{(k)}$.

Following the Lagrangian multiplier approach, the shape gradient with respect to the design parameter τ can be derived using the adjoint method (Wang and Turteltaub 2015, Wang and Kumar 2017). Given the objective function in Eq. (11), in order to satisfy the equality constraints from the equilibrium condition in Eq. (4) for any point $\boldsymbol{X} \in \Omega^{\tau}$ at each target strain α, an augmented functional is introduced as

$$\tilde{\Phi} = \Phi + \sum_{\alpha=1}^{\beta}\{\langle \boldsymbol{c}[\boldsymbol{u}], \boldsymbol{u}^{*}\rangle_{\Omega^{\tau}}\}_{\alpha}, \tag{12}$$

where $\langle \boldsymbol{c}[\boldsymbol{u}], \boldsymbol{u}^{*}\rangle_{\Omega^{\tau}} = \int_{\Omega^{\tau}} \boldsymbol{u}^{*} \cdot (\operatorname{div} \boldsymbol{P})\, \mathrm{d}\Omega = -\int_{\Omega^{\tau}} \boldsymbol{P} : \nabla \boldsymbol{u}^{*}\, \mathrm{d}\Omega + \int_{\Gamma^{\tau}} \boldsymbol{t} \cdot \boldsymbol{u}^{*}\, \mathrm{d}\Gamma$.

The Lagrange multiplier $\boldsymbol{u}^{*}$ is the so called adjoint displacement field and $\boldsymbol{t}$ is the traction on boundary Γ^{τ}. Recalling that $\hat{\boldsymbol{t}} = \boldsymbol{0}$ on Γ_t^{τ}, gives

$$\langle \boldsymbol{c}[\boldsymbol{u}], \boldsymbol{u}^{*}\rangle_{\Omega^{\tau}} = -\int_{\Omega^{\tau}} \boldsymbol{P} : \nabla \boldsymbol{u}^{*}\, \mathrm{d}\Omega + \int_{\Gamma_u^{\tau}} \boldsymbol{t} \cdot \boldsymbol{u}^{*}\, \mathrm{d}\Gamma. \tag{13}$$

The next step is to derive the total derivative of Eq. (12) with respect to design parameter τ

$$\dot{\tilde{\Phi}} = \frac{\mathrm{D}\tilde{\Phi}}{\mathrm{D}\tau} = \dot{\Phi} + \sum_{\alpha=1}^{\beta}\left\{\frac{\mathrm{D}}{\mathrm{D}\tau}\langle \boldsymbol{c}[\boldsymbol{u}], \boldsymbol{u}^{*}\rangle_{\Omega^{\tau}}\right\}_{\alpha}, \tag{14}$$

where $(\dot{\ }) = \frac{\mathrm{D}(\ )}{\mathrm{D}\tau}$ represents the *total* design derivative.

Given a continuous differentiable function h defined in Ω^τ and Γ^τ, the volume and surface transport relations are given, respectively, as

$$\frac{\mathrm{D}}{\mathrm{D}\tau}\int_{\Omega^\tau} h \,\mathrm{d}\Omega = \int_{\Omega^\tau} h' \,\mathrm{d}\Omega + \int_{\Gamma^\tau} h v_n \,\mathrm{d}\Gamma, \text{ and} \tag{15}$$

$$\frac{\mathrm{D}}{\mathrm{D}\tau}\int_{\Gamma^\tau} h \,\mathrm{d}\Gamma = \int_{\Gamma^\tau}(h' + \nabla h \cdot \boldsymbol{n} v_n - \kappa h v_n)\,\mathrm{d}\Gamma, \tag{16}$$

where $(\ )'$ denotes the *partial* design derivative, κ is the total curvature, $\boldsymbol{v}$ is the so-called design velocity at $\boldsymbol{X}$ defined as

$$\boldsymbol{v} = \dot{\boldsymbol{X}}[\tau] = \frac{\mathrm{D}\boldsymbol{X}[\tau]}{\mathrm{D}\tau}, \tag{17}$$

and $v_n = \boldsymbol{v}\cdot\boldsymbol{n}$, in which $\boldsymbol{n}$ is the unit outward normal vector.

Using the transport relation in Eq. (16), the first term on the right side of Eq. (14) can be written as

$$\dot{\Phi} = \sum_{\alpha=1}^{\beta}\left\{\sum_k \frac{1}{(E_{11}W)^2}(2\cdot(u_2 - \overline{u_2})\cdot u_2')_k\right\}_\alpha + \sum_{\alpha=1}^{\beta}\left\{\sum_k \frac{1}{(E_{11}W)^2}\left(\nabla((u_2 - \overline{u_2})^2)\cdot n_y v_n - k((u_2-\overline{u_2})^2)v_n\right)_k\right\}_\alpha. \tag{18}$$

Similarly, using the transport relations in Eqs. (15) and (16), the derivative of the second term on the right side of Eq. (12) becomes

$$\sum_{\alpha=1}^{\beta}\left\{\frac{D}{D\tau}\langle \boldsymbol{c}[\boldsymbol{u}], \boldsymbol{u}^*\rangle_{\Omega^\tau}\right\}_\alpha = \sum_{\alpha=1}^{\beta}\left\{-\int_{\Omega^\tau}\boldsymbol{P}' : \nabla\boldsymbol{u}^*\,\mathrm{d}\Omega - \int_{\Gamma^\tau}(\boldsymbol{P}:\nabla\boldsymbol{u}^*)v_n\,\mathrm{d}\Gamma + \int_{\Gamma_u^\tau}\boldsymbol{t}'\cdot\boldsymbol{u}^*\,\mathrm{d}\Gamma\right\}_\alpha + \sum_{\alpha=1}^{\beta}\left\{\int_{\Gamma_u^\tau}(\nabla(\boldsymbol{t}\cdot\boldsymbol{u}^*)\cdot\boldsymbol{n}v_n - k(\boldsymbol{t}\cdot\boldsymbol{u}^*)v_n)\,\mathrm{d}\Gamma\right\}_\alpha, \tag{19}$$

where the relation $\langle \boldsymbol{c}[\boldsymbol{u}], \boldsymbol{u}^{*\prime}\rangle_{\Omega^\tau} = 0$ is utilized to give

$$-\int_{\Omega^\tau}\boldsymbol{P}:\nabla\boldsymbol{u}^{*\prime}\,d\Omega + \int_{\Gamma_u^\tau}\boldsymbol{t}\cdot\boldsymbol{u}^{*\prime}\,\mathrm{d}\Gamma = 0. \tag{20}$$

From Eqs. (18) and (19), Eq. (14) can be rewritten as

$$\dot{\tilde{\Phi}} = \Psi_1 + \Psi_2, \tag{21}$$

where $\Psi_1 = \sum_{\alpha=1}^{\beta}\left\{-\int_{\Omega^\tau}\boldsymbol{P}':\nabla\boldsymbol{u}^*\,\mathrm{d}\Omega + \int_{\Gamma_u^\tau}\boldsymbol{t}'\cdot\boldsymbol{u}^*\,\mathrm{d}\Gamma + \sum_k \frac{1}{(E_{11}W)^2}(2\cdot(u_2-\overline{u_2})\cdot u_2')_k\right\}_\alpha$,

and

$$\Psi_2 = \sum_{\alpha=1}^{\beta}\left\{-\int_{\Gamma^\tau}(\boldsymbol{P}:\nabla\boldsymbol{u}^*)v_n\,\mathrm{d}\Omega + \int_{\Gamma_u^\tau}(\nabla(\boldsymbol{t}\cdot\boldsymbol{u}^*)\cdot\boldsymbol{n}v_n - k(\boldsymbol{t}\cdot\boldsymbol{u}^*)v_n)\,\mathrm{d}\Gamma + \sum_k \frac{1}{(E_{11}W)^2}\left(\nabla((u_2-\overline{u_2})^2)\cdot n_y v_n - k((u_2-\overline{u_2})^2)v_n\right)_k\right\}_\alpha.$$

Referring to the incremental constitutive relation $P' = \mathbb{C}:\nabla\boldsymbol{u}'$, Ψ_1 can be written as

$$\Psi_1 = \sum_{\alpha=1}^{\beta}\left\{\int_{\Omega^\tau}\mathrm{div}(\mathbb{C}:\nabla\boldsymbol{u}^*)\cdot\boldsymbol{u}'\,\mathrm{d}\Omega - \int_{\Gamma^\tau}(\mathbb{C}:\nabla\boldsymbol{u}^*)\boldsymbol{n}\cdot\boldsymbol{u}'\,\mathrm{d}\Gamma + \int_{\Gamma_u^\tau}\boldsymbol{t}'\cdot\boldsymbol{u}^*\,\mathrm{d}\Gamma\right\}_\alpha + \sum_{\alpha=1}^{\beta}\left\{\sum_k \frac{1}{(E_{11}W)^2}(2\cdot(u_2-\overline{u_2})\cdot u_2')_k\right\}_\alpha, \tag{22}$$

where $\mathbb{C}$ is the material tangent modulus.

In order to eliminate the implicitly dependent terms u_2' and $\boldsymbol{t}'$ in Eq. (22), displacement based adjoint BVPs, each corresponding to a target strain α, are introduced such that

$$\begin{cases} \boldsymbol{c}^*[\boldsymbol{u}^*] \coloneqq \mathrm{div}\,(\mathbb{C}:\nabla\boldsymbol{u}^*) = \boldsymbol{0} & \text{in } \Omega^\tau \\ (\mathbb{C}:\nabla\boldsymbol{u}^*)\boldsymbol{n} - \hat{\boldsymbol{t}}^* = 0;\ \hat{\boldsymbol{t}}^* = \left[0, \frac{1}{(E_{11}W)^2}\cdot 2\cdot(u_2-\overline{u_2})\right]^T & \text{on } \Gamma_{t^*}^\tau \\ \hat{\boldsymbol{t}}^* = (\mathbb{C}:\nabla\boldsymbol{u}^*)\boldsymbol{n} = 0 & \text{on } \Gamma_t^\tau \\ \boldsymbol{u}^{*+} = \boldsymbol{u}^{*-} & \text{on } \Gamma_u^\tau \end{cases} \tag{23}$$

in which $\hat{\boldsymbol{t}}^*$ is the prescribed adjoint traction along the boundary $\Gamma_{t^*}^\tau$ comprising of the $k(= 2, 3, 5, 6)$ master control points (refer to Fig. 2). The adjoint BVP formulated for a given target strain α is solved using the tangent stiffness operator of the primary BVP at equilibrium, as described in (Santos and Choi 1962).

Utilizing the adjoint model, Ψ_1 reduces to

$$\Psi_1 = \sum_{\alpha=1}^{\beta} \left\{ \int_{\Gamma_u^\tau - \Gamma_{t^*}^\tau} \boldsymbol{t}^* \cdot \boldsymbol{u}' \, \mathrm{d}\Gamma + \int_{\Gamma_u^\tau} \boldsymbol{t}' \cdot \boldsymbol{u}^* \, \mathrm{d}\Gamma \right\}_\alpha , \tag{24}$$

Considering that u' and u^* are periodic while t' and t^* are anti-periodic for the primary and adjoint BVPs, gives $\Psi_1 = 0$. Since the design velocity $\boldsymbol{v}$ is non-vanishing on the design boundary Γ_d^τ, the shape gradient in Eq. (14) reduces to

$$\frac{\mathrm{D}\tilde{\Phi}}{\mathrm{D}\tau} = \sum_{\alpha=1}^{\beta} \left\{ - \int_{\Omega^\tau} (\boldsymbol{P} : \nabla \boldsymbol{u}^*) v_n \, \mathrm{d}\Gamma \right\}_\alpha . \tag{25}$$

Following Eq. (5), the design velocity can be discretized as

$$\boldsymbol{v} = R^{ij}[\boldsymbol{X}] \frac{\mathrm{D}\boldsymbol{X}^{ij}[\tau]}{\mathrm{D}\tau} . \tag{26}$$

Substituting Eq. (26) into Eq. (25), the discretized isogeometric shape gradient with respect to the design control point $\boldsymbol{X}^{ij}$ can be obtained as

$$\Phi_{,\boldsymbol{X}^{ij}} = \frac{\partial \Phi}{\partial \boldsymbol{X}^{ij}} = \sum_{\alpha=1}^{\beta} \left\{ \int_{\Gamma_d^\tau} R^{ij} (-\boldsymbol{P} : \nabla \boldsymbol{u}^*) \boldsymbol{n} \, \mathrm{d}\Gamma \right\}_\alpha . \tag{27}$$

By solving for the unknown displacement fields $\boldsymbol{u}$ and $\boldsymbol{u}^*$ in the primary and adjoint problems, respectively, the discretized shape derivatives in Eq. (27) can be determined. The shape gradient is normalized to ensure the balance movement of the boundary design control points (Kiendl et al. 2014) and is given as

$$\hat{\Phi}_{,\boldsymbol{X}^{ij}} = \frac{\Phi_{,\boldsymbol{X}^{ij}}}{\int_{\Gamma_d^\tau} R^{ij} \mathrm{d}\Gamma} \tag{28}$$

3.2. Geometrical Constraints

The shape gradient obtained from Eq. (28) will result to a non-symmetric petals design and thus exhibits distinct behavior when loaded along two orthogonal directions. Hence, a symmetry constraint is necessary to preserve the geometrical symmetry of petal auxetics during shape optimization. The approach presented in Wang et al. (2017b) is adopted in this study.

The above-mentioned symmetric constraint, by itself, may result in a design with thin and weak connecting parts, which are difficult to manufacture. Consequently, it is necessary to impose a thickness constraint for the petals. Following polynomial-based thickness constraint presented in Wang et al. (2017b), an improved spline-spline based thickness constraint is developed in this study. The spline-based thickness constraint is accurate in terms of curve fitting the points generated to impose thickness constraint for a smooth petal shape.

4. RESULTS

In this section, the above-mentioned optimization formulation is utilized to design petal auxetics with different prescribed Poisson's ratios in the nonlinear regime. The first part focuses on designing tri-petal auxetics to achieve different values of constant Poisson's ratio up to 30% strain in plane strain condition. In the second part, hexa-petal auxetics are designed for prescribed constant Poisson's ratios within 30% strain in plane stress condition.

For the optimization, the geometrical specifications of the petal auxetics are as follows: the area of the RVE is chosen as 800 and 400 for tri-and hexa-petal structures. The connecting bars between the petals have fixed thickness of 1. The minimum thickness of petal arms is set to 0.20 to ensure manufacturability of the optimized designs.

4.1. Smoothed Tri-petals Structures with Constant Poisson's Ratio in Plane Strain

This subsection describes the design of tri-petals structures with different targeted constant Poisson's ratios up to 30% strain in plane strain condition. The design optimization of the smoothed tri-petals structure begins with an initial design having uniform petal thickness of 1 and a fixed interior boundary as depicted in Fig. 3(a).

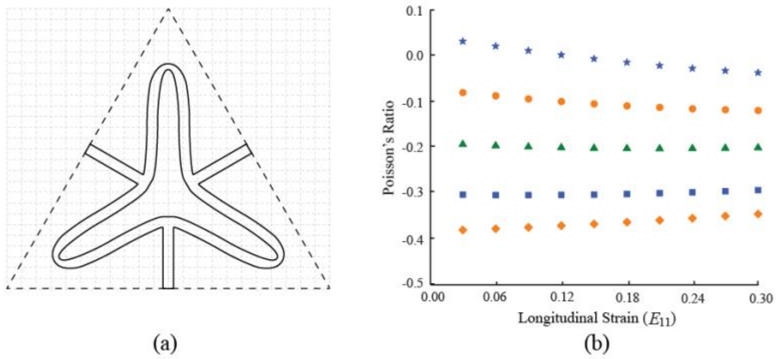

Figure 3. Smoothed tri-petals structure: (a) Initial design, (b) Performance of optimized structures with various prescribed constant Poisson's ratios. Note that only half of tri-petals RVE is shown in (a).

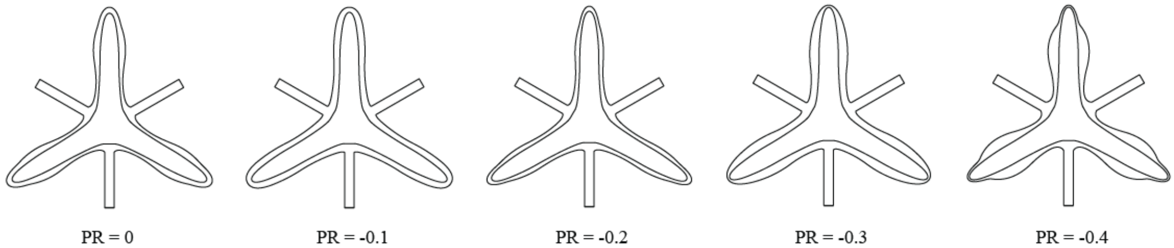

Figure 4. Optimized smoothed tri-petals structures with different constant Poisson's ratios up to 30% strain in plane strain.

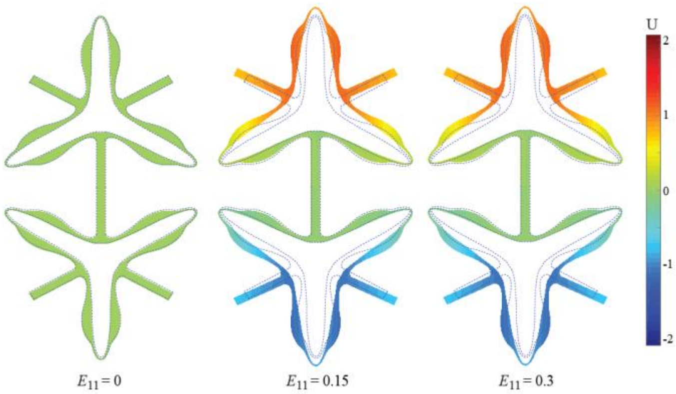

Figure 5. Resultant displacement (U) contour plot of deformed optimized tri-petals RVE with constant Poisson's ratio of -0.4 up to 30% in plane strain.

The smoothed tri-petals structure is optimized for different targeted Poisson's ratio of $\nu \subset \{0, -0.1, -0.2, -0.3, -0.4\}$. The performance of the optimized tri-petals structures is summarized in Fig. 3(b), where the Poisson's ratios are close to the target Poisson's ratios in the desired strain interval. The optimized tri-petals structures are shown in Fig. 4. The deformed configurations of the optimized structure with a Poisson's ratio of -0.4, at 15% and 30% strains are shown in Fig. 5. It can be observed that the auxetic behavior of smoothed tri-petals is induced by the opening of the petals, together with the movement of connecting bars.

4.2. Smoothed Hexa-petals Structures with Constant Poisson's Ratio in Plane Stress

The presentation here focuses at designing hexa-petals structures with different prescribed constant Poisson's ratios up to 30% strain in plane stress condition. The design optimization of the smoothed hexa-petals structure begins with an initial design having uniform petal thickness of 0.8 and a fixed interior boundary as depicted in Fig. 6(a).

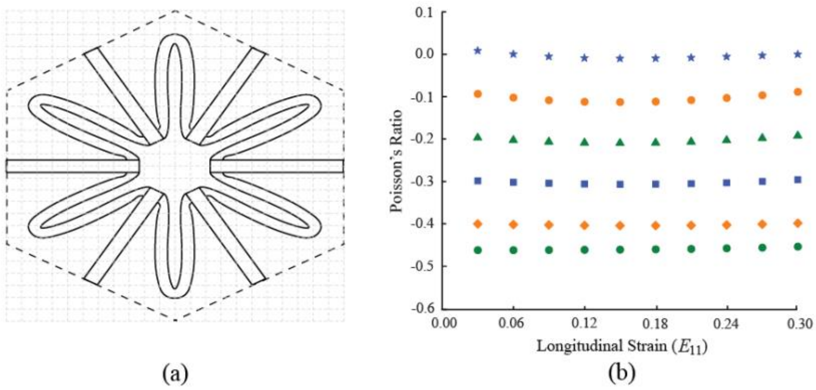

Figure 6. Smoothed hexa-petals structure: (a) Initial design, (b) Performance of optimized structures with various prescribed constant Poisson's ratios.

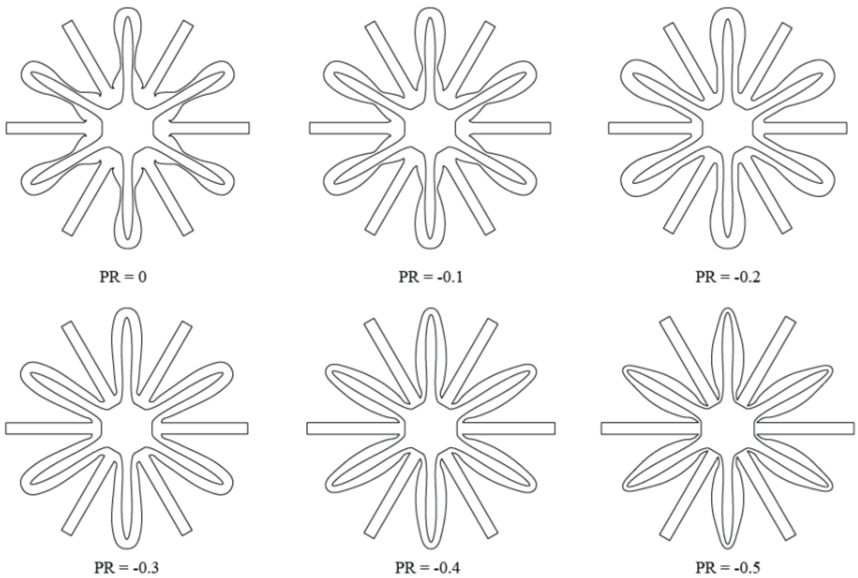

Figure 7. Optimized smoothed hexa-petals structures with different constant Poisson's ratios up to 30% strain in plane stress.

The smoothed hexa-petals structure is optimized for different targeted Poisson's ratio of $\nu \subset \{0, -0.1, -0.2, -0.3, -0.4, -0.5\}$. The performance of the optimized hexa-petals structures is summarized in Fig. 6(b), where the Poisson's ratios are close to the target Poisson's ratios in the desired strain interval. The optimized hexa-petals structures are shown in Fig. 7. The deformed configurations of the optimized structure with a Poisson's ratio of -0.5, at 15% and 30% strains are shown in Fig. 8. It can be seen from Fig. 8 that the initial auxetic behavior is due to the opening of two petals along the vertical axis of symmetry. Subsequently, the opening of other four petals triggers the auxetic behavior at very large strains.

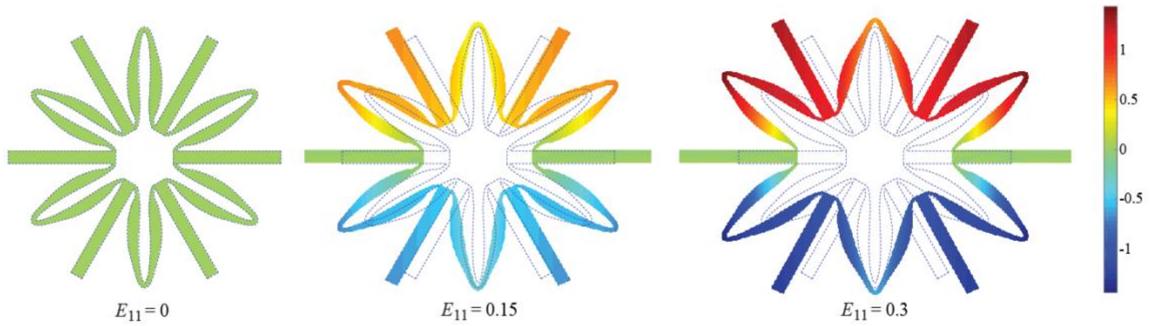

Figure 8. Resultant displacement (U) contour plot of deformed optimized hexa-petals RVE with constant Poisson's ratio of -0.5 up to 30% in plane stress.

5. CONCLUSIONS

In this paper, an isogeometric shape optimization framework to design smoothed petals auxetics with prescribed nonlinear deformation is presented. Geometry constrains are imposed to ensure symmetry and manufacturability of the optimized designs. The exterior boundary of smoothed tri- and hexa-petals structures is optimized to obtain a series of smoothed petals structures with different constant Poisson's ratios within -0.5. Numerical results demonstrate that the optimized designs can achieve nearly constant Poisson's ratios up to 30% strain in both plane strain and plane stress conditions.

REFERENCES

Alderson, A., 1999. A triumph of lateral thought. *Chemistry & Industry*, *17*, pp.384-391.

Alderson, K.L., Fitzgerald, A. and Evans, K.E., 2000. The strain dependent indentation resilience of auxetic microporous polyethylene. *Journal of Materials Science*, *35*(16), pp.4039-4047.

Babaee, S., Shim, J., Weaver, J.C., Chen, E.R., Patel, N. and Bertoldi, K., 2013. 3D soft metamaterials with negative Poisson's ratio. *Advanced Materials*, *25*(36), pp.5044-5049.

Biot, M.A., 1939. XLIII. Non-linear theory of elasticity and the linearized case for a body under initial stress. *The London, Edinburgh, and Dublin Philosophical Magazine and Journal of Science*, *27*(183), pp.468-489.

Carneiro, V.H., Puga, H. and Meireles, J., 2016. Analysis of the geometrical dependence of auxetic behavior in reentrant structures by finite elements. *Acta Mechanica Sinica*, *32*(2), pp.295-300.

Cho, S. and Ha, S.H., 2009. Isogeometric shape design optimization: exact geometry and enhanced sensitivity. *Structural and Multidisciplinary Optimization*, *38*(1), p.53.

Choi, M.J. and Cho, S., 2018. Isogeometric configuration design optimization of shape memory polymer curved beam structures for extremal negative poisson's ratio. *Structural and Multidisciplinary Optimization*, *58*(5), pp.1861-1883.

Choi, K.K. and Kim, N.H., 2006. *Structural Sensitivity Analysis and Optimization 1: Linear Systems*. Springer Science & Business Media.

Clausen, A., Wang, F., Jensen, J.S., Sigmund, O. and Lewis, J.A., 2015. Topology optimized architectures with programmable Poisson's ratio over large deformations. *Advanced Materials*, *27*(37), pp.5523-5527.

Da, D., Yvonnet, J., Xia, L., Le, M.V. and Li, G., 2018. Topology optimization of periodic lattice structures taking into account strain gradient. *Computers & Structures*, *210*, pp.28-40.

Dirrenberger, J., Forest, S. and Jeulin, D., 2013. Effective elastic properties of auxetic microstructures: anisotropy and structural applications. *International Journal of Mechanics and Materials in Design*, *9*(1), pp.21-33.

Hughes, T.J., Cottrell, J.A. and Bazilevs, Y., 2005. Isogeometric analysis: CAD, finite elements, NURBS, exact geometry and mesh refinement. *Computer Methods in Applied Mechanics and Engineering*, *194*(39-41), pp.4135-4195.

Kaminakis, N.T., Drosopoulos, G.A. and Stavroulakis, G.E., 2015. Design and verification of auxetic microstructures using topology optimization and homogenization. *Archive of Applied Mechanics*, *85*(9-10), pp.1289-1306.

Kiendl, J., Schmidt, R., Wüchner, R. and Bletzinger, K.U., 2014. Isogeometric shape optimization of shells using semi-analytical sensitivity analysis and sensitivity weighting. *Computer Methods in Applied Mechanics and Engineering*, *274*, pp.148-167.

Kumar, D., Wang, Z.P., Poh, L.H. and Quek, S.T., 2019. Isogeometric shape optimization of smoothed petal auxetics with prescribed nonlinear deformation. *Computer Methods in Applied Mechanics and Engineering*, *356*, pp.16-43.

Lakes, R., 1991. Deformation mechanisms in negative Poisson's ratio materials: structural aspects. *Journal of Materials Science*, *26*(9), pp.2287-2292.

Lian, H., Kerfriden, P. and Bordas, S.P., 2016. Implementation of regularized isogeometric boundary element methods for gradient-based shape optimization in two-dimensional linear elasticity. *International Journal for Numerical Methods in Engineering*, *106*(12), pp.972-1017.

Lian, H., Christiansen, A.N., Tortorelli, D.A., Sigmund, O. and Aage, N., 2017. Combined shape and topology optimization for minimization of maximal von Mises stress. *Structural and Multidisciplinary Optimization*, *55*(5), pp.1541-1557.

Liu, J. and Zhang, Y., 2018. Soft network materials with isotropic negative Poisson's ratios over large strains. *Soft Matter*, *14*(5), pp.693-703.

Ma, Q., Cheng, H., Jang, K.I., Luan, H., Hwang, K.C., Rogers, J.A., Huang, Y. and Zhang, Y., 2016. A nonlinear mechanics model of bio-inspired hierarchical lattice materials consisting of horseshoe microstructures. *Journal of the Mechanics and Physics of Solids*, *90*, pp.179-202.

Nguyen, V.P., Anitescu, C., Bordas, S.P. and Rabczuk, T., 2015. Isogeometric analysis: an overview and computer implementation aspects. *Mathematics and Computers in Simulation*, *117*, pp.89-116.

Santos, J.L. and Choi, K.K., 1992. Shape design sensitivity analysis of nonlinear structural systems. *Structural Optimization*, *4*(1), pp.23-35.

Schwerdtfeger, J., Wein, F., Leugering, G., Singer, R.F., Körner, C., Stingl, M. and Schury, F., 2011. Design of auxetic structures via mathematical optimization. *Advanced Materials*, *23*(22-23), pp.2650-2654.

Sigmund, O., 1994. Materials with prescribed constitutive parameters: an inverse homogenization problem. *International Journal of Solids and Structures*, *31*(17), pp.2313-2329.

Sigmund, O., 1995. Tailoring materials with prescribed elastic properties. *Mechanics of Materials*, *20*(4), pp.351-368.

Smith, C.W., Wootton, R.J. and Evans, K.E., 1999. Interpretation of experimental data for Poisson's ratio of highly nonlinear materials. *Experimental Mechanics*, *39*(4), pp.356-362.

Spadoni, A., Ruzzene, M., Gonella, S. and Scarpa, F., 2009. Phononic properties of hexagonal chiral lattices. *Wave Motion*, *46*(7), pp.435-450.

Sun, S.H., Yu, T.T., Nguyen, T.T., Atroshchenko, E. and Bui, T.Q., 2018. Structural shape optimization by IGABEM and particle swarm optimization algorithm. *Engineering Analysis with Boundary Elements*, *88*, pp.26-40.

Vogiatzis, P., Chen, S., Wang, X., Li, T. and Wang, L., 2017. Topology optimization of multi-material negative Poisson's ratio metamaterials using a reconciled level set method. *Computer-Aided Design*, *83*, pp.15-32.

Wall, W.A., Frenzel, M.A. and Cyron, C., 2008. Isogeometric structural shape optimization. *Computer Methods in Applied Mechanics and Engineering*, *197*(33-40), pp.2976-2988.

Wang, Y., Gao, J., Luo, Z., Brown, T. and Zhang, N., 2017. Level-set topology optimization for multimaterial and multifunctional mechanical metamaterials. *Engineering Optimization*, *49*(1), pp.22-42.

Wang, F., Sigmund, O. and Jensen, J.S., 2014. Design of materials with prescribed nonlinear properties. *Journal of the Mechanics and Physics of Solids*, *69*, pp.156-174.

Wang, Z.P. and Kumar, D., 2017. On the numerical implementation of continuous adjoint sensitivity for transient heat conduction problems using an isogeometric approach. *Structural and Multidisciplinary Optimization*, *56*(2), pp.487-500.

Wang, Z.P., Poh, L.H., Dirrenberger, J., Zhu, Y. and Forest, S., 2017. Isogeometric shape optimization of smoothed petal auxetic structures via computational periodic homogenization. *Computer Methods in Applied Mechanics and Engineering*, *323*, pp.250-271.

Wang, Z.P. and Poh, L.H., 2018. Optimal form and size characterization of planar isotropic petal-shaped auxetics with tunable effective properties using IGA. *Composite Structures*, *201*, pp.486-502.

Wang, Z.P. and Turteltaub, S., 2015. Isogeometric shape optimization for quasi-static processes. *International Journal for Numerical Methods in Engineering*, *104*(5), pp.347-371.

Weeger, O., Narayanan, B. and Dunn, M.L., 2019. Isogeometric shape optimization of nonlinear, curved 3D beams and beam structures. *Computer Methods in Applied Mechanics and Engineering*, *345*, pp.26-51.

Xia, L., Xia, Q., Huang, X. and Xie, Y.M., 2018. Bi-directional evolutionary structural optimization on advanced structures and materials: a comprehensive review. *Archives of Computational Methods in Engineering*, *25*(2), pp.437-478.

Xie, X., Wang, S., Xu, M. and Wang, Y., 2018. A new isogeometric topology optimization using moving morphable components based on r-functions and collocation schemes. *Computer Methods in Applied Mechanics and Engineering*, *339*, pp.61-90.

Yeoh, O.H., 1993. Some forms of the strain energy function for rubber. *Rubber Chemistry and technology*, *66*(5), pp.754-771.

Zhu, Y., Wang, Z.P. and Poh, L.H., 2018. Auxetic hexachiral structures with wavy ligaments for large elasto-plastic deformation. *Smart Materials and Structures*, *27*(5), p.055001.

Zhu, Y., Zeng, Z., Wang, Z.P., Poh, L.H. and Shao, Y., 2019. Hierarchical hexachiral auxetics for large elasto-plastic deformation. *Materials Research Express*, *6*(8), p.085701.

ACKNOWLEDGEMENTS

The work presented in this paper is supported by the MOE Tier 2 Grant R302000139112.